On-orbit spectral calibration for dispersive imaging spectrometer using back-illuminated CCDs

MA Liang， WEI Jun， HUANG Xiao-Xian

(Shanghai Institute of Technical Physics of the Chinese Academy of Sciences，Shanghai 200083，China)

Abstract：Dispersive imaging spectrometers that use back-illuminated CCDs have interference fringes in near-infrared band. These fringes are sensitive to the distribution of incident light wavelength and stable in spatial frequency. Therefore，they are very suitable for measuring and calibrating spectral deviation. In this paper，we built a grating dispersion push-broom imaging spectrometer prototype. We then estimated the distribution law of fringes and use band-pass filter and least squares method to extract the phase information of the interference fringes. Finally，we calculated the spectrum offsets based on this information. Experiments show that when the incident light intensity changes by more than 130%，the maximum uncertainty of fitting line positions is 0. 007 3 nm. We change the spectral position and compare the spectral deviations calculated by using fitting algorithm and measured by using mercury spectrum. The maximum error of spectral position is 0. 135 8 nm. Our fitting algorithm can effectively reduce dependence on light stability of the calibration system，and improve detection accuracy for slight offsets in spectral dimension.

Key words：spectral calibration，back-illuminated，interference，imaging spectrometer
PACS：07. 57. Ty

一种针对使用背照减薄型 CCD 器件色散型成像光谱仪的星上光谱定标方法

马 亮， 危 峻， 黄小仙
(中国科学院上海技术物理研究所,上海 200083)

摘要：使用背照减薄型 CCD 器件的色散型成像光谱仪在近红外波段会出现呈条带状干涉条纹现象,该干涉条纹对入射光波长分布敏感,空间频率稳定,特别适用于微小光谱偏差的测量与校准。针对一台光栅色散型推扫式成像光谱仪样机,先估计出条纹分布的规律,再以此为基础,采用频域滤波、最小二乘拟合等方法提取干涉条纹中包含的相位信息,以此作为光谱定标的辅助参数。实验表明,当入射光强变化达到 130% 以上时,拟合谱线位置的不确定度最大为 0. 007 3 nm,模拟光谱位置改变后,以汞灯谱线作为基准光谱位置曲线,测得拟合算法的最大误差为 0. 135 8 nm,该结果证明,干涉条纹拟合定标方法可有效减少定标系统对光源稳定性的依赖,提高对光谱维微小偏移量的检测精度。

关 键 词：光谱定标；被照减薄；干涉条纹；成像光谱仪
中图分类号：O436. 1   **文献标识码**：A

Introduction

Imaging spectrometer technology，which emerged late last century，is a new remote sensing method based on hyperspectral remote sensing technology. Given its ability to obtain target high-resolution images with high spectral resolution，this technology has been widely used in Earth observation from space[1-4].

Usually，imaging spectrometers have a spectral resolution of less than 10 nm and narrow observation channels of more than tens or even hundreds. Spectra acqui-

sition must be accurate and repeatable. Therefore, in order to establish the relationship between the amount of entering radiation and the output signal, the imaging spectrometer has to be spectrum-calibrated and radiation-calibrated strictly[5-8]. In many space applications, only MODIS [9] in America uses a monochromator as an on-orbit spectral calibration device, whereas others calibrate the center wavelengths of imaging spectrometer observation channels by known characteristic lines during flight on orbit [10]. For example, Hyperion on EO-1 uses a calibration board which has an absorption wavelength that is typically serves as basis [11-12]. Green *et al*. achieved the spectral calibration of AVIRIS by using spectral radiance matching [13-14]. Gao *et al*. calculated the central wavelength offset of Hyperion, AVIRIS, and PHILLS by using a spectral matching algorithm without measured surface reflectance [15]. In general, what these methods have in common is that they calculate the offset of the spectrum curve by comparing the measured spectral lines with the known lines according to some algorithms. Thus, the estimation of known spectral lines must be accurate, and line distribution must remain stable during flight on orbit. For instance, when a characteristic absorption glass is used, the absorption peak position of the light and the glass should be kept stable [16].

According to different spectrometer methods, imaging spectrometers can be divided into dispersive type (including prism dispersive type and grating dispersion type), Fourier transform type, tunable filter type, optical wedge imaging type, and tomography imaging type. Among these methods, dispersive imaging technology is mature and most widely used[17-18]. When dispersive imaging spectrometers use a back-illuminated CCD device, unique interference fringes appear in the near-infrared band [19]. The spatial frequency of these fringes has a relationship with the spectral position of the imaging spectrometer and the physical property of the detector surface. In addition, these fringes are very sensitive to the wavelength of the incident light but are unaffected by spatial and spectral distribution of light intensity. Thus, these fringes can reduce the requirements of known spectral stability and is adequate for the measurement and calibration of slight spectrum deviation.

1   Principle of interference fringes

Figure 1 shows the phenomenon of interference fringes observed by using a grating dispersion push-broom imaging spectrometer prototype. Its horizontal direction is the direction across the track (i. e., the spatial dimension), and its vertical direction is the direction parallel to the track (i. e. the spectral dimension). In the vertical direction, the incident wavelength increases from the bottom to the top, and we can find the dark and light interference fringes changing with the incident wavelength in Fig. 1.

Figure 2 is a schematic diagram of the front-side and the back-illuminated CCDs. The diagram on the left is the front-side CCD, in which light normally enters through the gates of the parallel register. These gates are made of very thin polysilicon, which is reasonably transparent at long wavelengths. However, this polysilicon
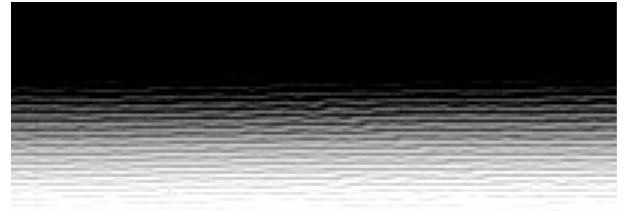

Fig. 1   Interference fringe pattern from 867 nm to 1 042 nm
图1   867 ~ 1 042 nm 波段实际产生的干涉条纹图

becomes opaque at wavelengths shorter than 400 nm. Thus, quantum efficiency (QE) declines at short wavelengths. The diagram on the right is the back-illuminated CCD, which focuses an image on the backside where no gate structure exists. Usually, back-illuminated CCD's thickness is about 10 μm to 20 μm. This thickness can increase QE, but bring in interference fringes above the 750 nm band. In this band, the light absorption efficiency of silicon material declines rapidly. When the incident light passes through the sensitive part of the CCD, it cannot be absorbed completely but is reflected back and forth between the two surfaces of the photosensitive region. Thus, the interference phenomenon appeared as shown in Fig. 1 [20-22].

Based on the above analysis, the principle of the interference fringes is similar to that of the Fabry – Perot interferometer. Thus, the relationship between the incident wavelength and the thickness of the photosensitive area can be calculated by the multi-beam interference formula for parallel plates.

According to the longitudinal mode frequency formula,
$$2nL = m\lambda \quad m = 1,2,3,\cdots \qquad , \quad (1)$$
here, n is the refractive index of the CCD photosensitive area, L is the thickness of the photosensitive area, m is the interference progression, and λ is the wavelength. This formula yields Eq. (2) to calculate longitudinal mode spacing Δv_e.

$$v_e = v_m - v_{m-1} = \frac{c}{2nL} \qquad . \quad (2)$$

Before estimating the thickness of the photosensitive area of CCD, we have to know the spectral response curve of each row in CCD. Thus, we used a monochromator to scan from 600 nm to 1 010 nm, and then we obtained spectral response curves that correspond to each line in CCD. These curves are convolutions of the spectrum. Here, we choose their central values as the absolute wavelength of each line.

In sample photo column 505, there are a total of 31 bright stripes from row 233 to row 311. According to the results measured by the monochromator, the center wavelength is 1 007. 83 nm at row 233 and 814. 34 nm at row 246. By using Eq. (2), we can calculate longitudinal mode spacing $\Delta v_e = 0.707~3 \times 10^{14}$ H . By querying relevant manuals[23], we can find the refractive index distribution of silicon from 600 nm to 1 000 nm. From 814 nm to 1 008 nm, the refractive index changes by less than 0. 01. Thus, we choose $n = 3.673$ as the refractive near the response wavelength. The speed of light is 3 × 10^{14} μm/s. T. The thickness of the detector photosensitive near column 505 can be obtained as $L = 17.899$ μm, which conforms to the results of the design thickness (17 μm).
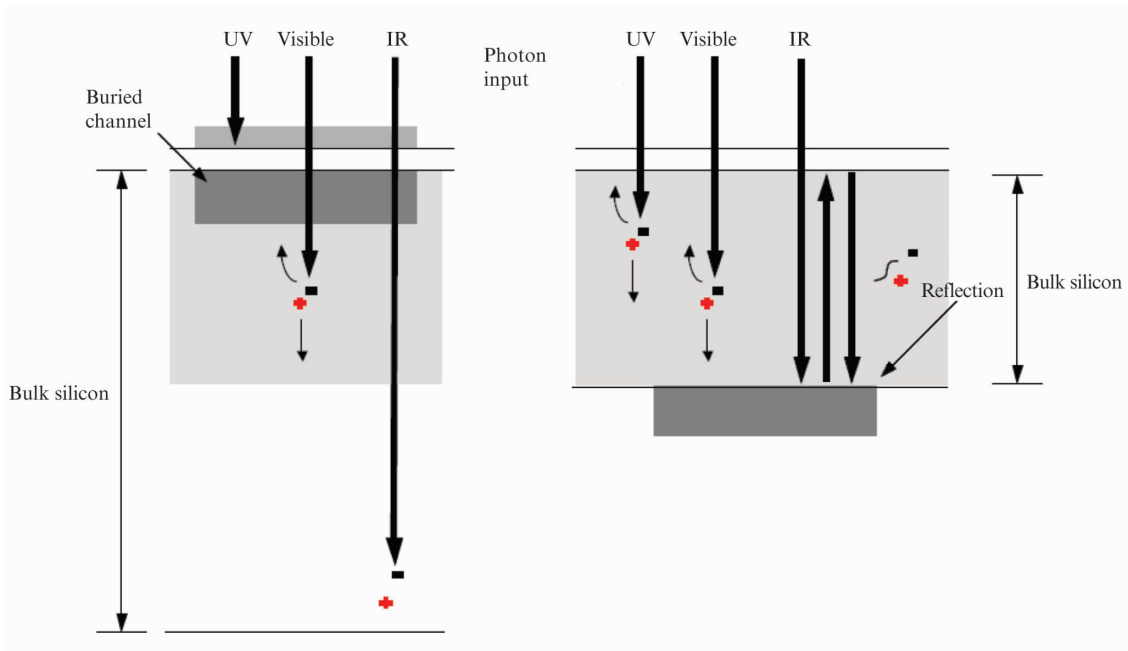
Fig. 2　Operation principle of CCDs（a）front-side CCD；（b）back-illuminated CCD

图 2　CCD 原理示意（a）前照型 CCD；（b）背照减薄型 CCD

2　Spectral calibration by interference fringes

From Eq.（1）, if the optical coefficient of the photosensitive surface material is distributed uniformly, the distribution of interference fringes is relevant only to the wavelength of the incident light and the detector's photosensitive area thickness distribution. Here, we assume that the entire detector surface is uniform. The case of a non-uniform detector surface is discussed later.

Figure 1 shows a picture obtained after splitting the incident light. In the horizontal direction, each row represents a particular wavelength. Theoretical and experimental results show that interference fringes appear at about 750 nm and become very obvious above 900 nm. By using Eq.（2）and assuming a uniform thickness distribution, we can calculate the wavelength difference between adjacent stripes as $d\lambda = 1/v_m - 1/v_{m-1}$. The curve in Fig. 3 shows that the intervals between adjacent stripes increase with the increasing wavelength of incident light. The dispersion of our test system is uniform, thus, the intervals between adjacent stripes increase smoothly and slowly. If a non-uniform spectral dispersion exists in the focal plane, the curve becomes steeper or flatter.

Ordinate $d\lambda$ is the wavelength interval of the adjacent stripe, whereas the abscissa is the wavelength of incident light. Both units are in nm.

The spectrometer prototype used in the test has a spatial frequency of 2.5 nm/pixels. To avoid under sampling, we choose a part of the picture whose spectral intervals of adjacent stripes are greater than 5 nm, that is, the sampling frequency is greater than two times the Nyquist frequency. As Fig. 3 shows, 10 columns are selected near 950 nm for the test.

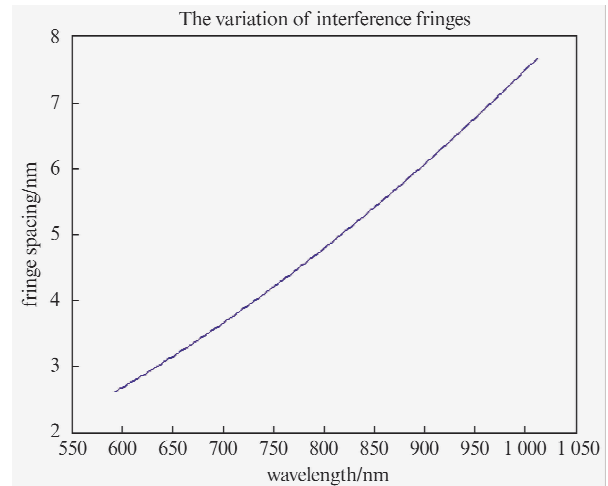At first, before using interference fringes for calibration, we need a mathematical model for the fringes.

Fig. 3　Variation of interference fringe interval

图 3　相邻条纹间隔随波长的变化图

Assuming that the actual image is $A(x,y)$ and the detector response image is $I(x,y)$, a relationship exists as Eq.（3）[24].

$$I(x,y) = A(x,y) + B(x,y)\cos\{\varphi(x,y)\} \quad ,(3)$$

$\varphi(x,y)$ is the phase angle of the interference fringes, and it changes continuously along the x and y directions. $B(x,y)$ is the superimposed magnitude response of the interference fringes. This response is only related to the incident light intensity $A(x,y)$ when the spectral position changes only slightly. Thus, Eq.（3）can be rewritten as Eq.（4）.

$$I(x,y) = A(x,y)\{1 + \delta(x,y)\cos[\varphi(x,y)]\} \quad ,(4)$$

here, $B(x,y) = A(x,y)\delta(x,y)$.

We then use the cosine function to simulate the response of the interference fringes. According to Fig. 3, the interval of the interference fringes changes with the

line position of y_0, and $\varphi(x,y)$ can be written as Eq. (5). Moreover, because $d\lambda$ changes slowly in narrow bandwidth, to simplify calculation, it can be represented by a constant value of λ_0. If a sharp change exists near λ_0 (for situations such as a non-uniform spectral dispersion), the approximation produces a great error.

$$\varphi(x,y_0) = \frac{2\pi}{d\lambda(y_0)} \cdot x + \varphi(y_0) \quad . \quad (5)$$

Integrating Eq. (5) into Eq. (4) yields Eq. (6).

$$I(x,y_0) = A(x,y_0) + A(x,y_0) \cdot$$
$$\delta(x,y_0)\cos\left\{\frac{2\pi}{d\lambda} \cdot x + \varphi(y_0)\right\} \quad , \quad (6)$$

In Eq. (6), $2\pi/d\lambda$ is the corner frequency of the interference fringes in column y_0, which is close to the wavelength λ_0. $\varphi(y_0)$ is the phase angle in column y_0 that contains the location information of that column on the spectral dimension.

On this basis, we suppose that $I(x,y)$ is the image for calibration, $I_F(x,y)$ is the image for fitting ($0 < x < m, 0 < y < n$), and the interference fringe interval equals $d\lambda$ near the wavelength λ_0. We then calculate the Fourier transform of $I(x,y)$ and build the filter $H(x,y)$ whose stop band is near $d\lambda$ to remove the components of the interference fringes. As a result, we can obtain the approximation of the actual image in Eq. (7).

$$A_F(x,y) = F^{-1}\{H(x,y)F[I(x,y)]\} \quad . \quad (7)$$

Given that $B(x,y)$ is stable in a certain range, to simplify calculation, we use B the peak of $I(x,y) - A_F(x,y)$, instead of $A(x,y)\delta(x,y)$. Finally, we obtain Eq. (8).

$$I_F(x,y) = A_F(x,y) + B \cdot \cos\left\{\frac{2\pi}{d\lambda} \cdot x + \varphi(y)\right\} \quad . \quad (8)$$

Finally, we use $I_F(x,y)$ to fit $I(x,y)$ by using the least squares method.

$$\chi^2(\varphi) = \sum_{y=0}^{n}\sum_{x=0}^{m} (I_F(x,y) - I(x,y))^2 \quad . \quad (9)$$

In Eq. (9), by changing $\varphi(y)$ and calculating $\chi^2(\varphi)$, we can find a group of $\varphi_0(y)$ that minimizes $\chi^2(\varphi)$. This group of $\varphi_0(y)$ represents the spectral phase value from column 0 to n. By setting these offset values as the start position of the spectrum, when spectral shift occurs, we can use these values to reposition the spectrum. The spectral offset is assumed to be $\Delta\lambda_k$ and $\Delta\lambda_n < \pm d\lambda/2$. With refitting by using Eq. (9), we can obtain a new group of $\varphi(y)$ as $\varphi_k(y)$. By multiplying $d\lambda/2\pi$ by the difference between $\varphi_0(y)$ and $\varphi_k(y)$, we can find the spectral shift by using Eq. (10).

$$\Delta\lambda_k = \frac{1}{n}\sum \frac{d\lambda}{2\pi}[\varphi_k(y) - \varphi_0(y)] \quad . \quad (10)$$

To sum up, compared with traditional spectral radiance direct matching, interference fringe fitting has the following advantage. The fitting process depending on Eq. (7) to Eq. (9) is actually band-pass filtering to the original image signal. After the interference signal is extracted separately, it can be used to calculate phase information by fitting algorithm. Thus, if the original signal has some additive and multiplicative interference $p_0(x,y)$ and $p_1(x,y)$, the original signal can be written as Eq. (11).

$$I(x,y) = p_1(x,y)A(x,y) + p_0(x,y) +$$
$$B(x,y)\cos\{\varphi(x,y)\} \quad , \quad (11)$$

$p_0(x,y)$ and $p_1(x,y)$ are assumed to have a smooth energy distribution in the frequency band. After $I_F(x,y) - I(x,y)$ in Eq. (9), the interference is then eliminated. In other words, when calculating the spectral shift, we just use the phase information of the interference fringes signal represented by a cosine function. The signal is a narrow band, and its frequency is known. Therefore, if we use a band-pass filter, we can not only extract the signal for calibration but also exclude the interference signal. On the contrary, the direct spectral radiance matching method is more sensitive to interference.

According to Eqs. (1) and (2), when the detector surface is completely flat, in the spectral dimension, interference fringes look like a series of parallel light and dark stripes whose intervals increase with the increase in the wavelength of interval light. When the thickness is uniformly distributed in the spatial dimension direction of the detector plane, this brings in slope and distortion in interference fringes. When the thickness is uniformly distributed in the spectrum dimension direction of the detector plane, the interval of interference fringes will increase unusually from the law in Fig. (3). Heterogeneity in spatial dimension just brings an additive interference p to the phase offset value in each column, as shown in $\varphi_0(y) + p$, which is removed in Eq. (9) when two offsets are subtracted. It has no effect on fitting accuracy. However, heterogeneity in the spectrum dimension leads to inaccurate estimates of the interval of interference fringes. Thus, the influence of heterogeneity in the spectrum dimension should be analyzed.

Given that the sampling frequency of the detector is not enough, the heterogeneity in the spectrum dimension is difficult to calculate directly. We estimate the heterogeneity in the spatial dimension first. After statistics for 45 interference fringes in 15 images, in 1 024 columns, the maximum offset of rows is 16 pixels. Single pixel spectral resolution is 2.5 nm/pixel thus, the maximum spectral offset in the horizontal direction is $16 \times 2.5/1 024 = 0.039$ nm. By Eq. (1), we know that m values are constant when the same spectral series exists. Thus, adjacent pixel maximum variation in thickness is shown in Eq. (12).

$$\Delta l = \frac{m \cdot \Delta\lambda}{2n} = 0.714 \text{ nm} \quad . \quad (12)$$

Generally, in either horizontal or vertical direction, the thickness distribution of the detector surface is consistent. In the actual test, we choose 10 points in the spectral dimension near 950 nm, and the maximum thickness variation is $10 \times 0.714 = 7.14$ nm. Eq. (13) is a deformation of Eq. (2).

$$\Delta\lambda = 2nL \cdot \frac{1}{m(m+1)} \quad , \quad (13)$$

$m \approx 138$. By using Eq. (13), we can calculate that $\Delta\lambda_1 = 6.855$ nm and $\Delta\lambda_2 = 6.857$ nm, which means that the maximum uncertainty of fringe interval that results from thickness uniformity is 0.002 nm. This value is much less than the expected calibration accuracy and can be ignored. If calibration accuracy is 0.02 nm, the calibration accuracy can deviate sufficiently given a uniformity of thickness of at least 53 nm in the vertical direction.

This result is higher than the maximum deviation of 1 024 pixels in the horizontal direction. Thus, this situation cannot exist absolutely.

3 Measurement results and analysis

Based on the periodicity of the cosine function, we can use this method to obtain accurate spectral offset $\Delta\lambda_n$ when spectral shift is smaller than $\pm\Delta\lambda/2$. That is particularly suitable for the identification of very small displacements in spectral dimension. When the spectral shift is greater than $\pm\Delta\lambda/2$, we can measure the direction and approximate value of the spectral shift at first by using PrNd glass, and then use interference fringe fitting to precisely locate the spectrum position.

Based on the analysis above, we built a grating dispersion push-broom imaging spectrometer prototype to test. The system used an integrating sphere with halogen lamps as observation target. Fig. 4 shows the schematic diagram of the prototype.
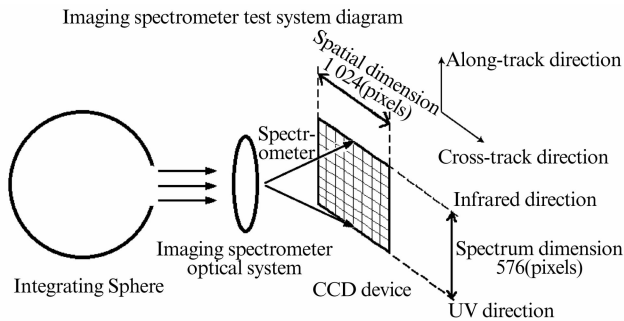

Fig. 4 Diagram of test system
图 4 测试系统示意图

The imaging spectrometer spectral range is 450 nm to 1 020 nm, its CCD is 1 024(space) ×576(spectral), the effective pixels are 250 lines, and the average spectral pixel interval is 2.5 nm. In Fig. 4, the vertical direction is the spectral dimension that corresponds to the direction along the track, whereas the horizontal direction is the spatial dimension that corresponds to the direction across the track. Other data about the spectrometer are shown in Table 1.

Table 1 Spectrometer prototype instrument performance
表 1 光谱仪原型机基本参数

Spectral performance	
Spectral range	400 ~ 1 020 nm
Spectral bands	250(unbinned)
Spectral sampling interval	2.5 nm
Spectral resolution(FWHM)	2.8 nm
Spatial pixels(across track)	1 024
FOV	14°
IFOV	0.25 mrad
Detector Characteristics	
Dynamic range	14 bit
Pixel size	22.5 μm square
Smile	Average < 0.8 pixel
Keystone	Average < 1.0 pixel
Coregistration	Average < 0.5 pixel
Maximum data rate	6 MHz
Charge storage capacity	600 000e⁻
Dark signal(at 0 ℃)	6 000e⁻/pixel/second

To verify that interference fringe calibration is insensitive to changes in light intensity, we used the spectrometer to observe the integrating sphere under different brightness, and then calculated the spectral shift starting position in 10 different columns by using interference fringe fitting. The results are shown in Table 2.

Table 2 Spectrum starting position under different light intensities after fitting
表 2 不同光源强度下拟合得到的谱线起始位置

Halogen Number	Column/nm									
	1 345	1 346	1 347	1 348	1 349	1 350	1 351	1 352	1 353	1 354
7	6.333	6.193	6.166	6.211	6.032	5.832	5.986	6.056	5.880	5.841
6	6.332	6.199	6.166	6.199	6.034	5.826	5.995	6.059	5.881	5.836
5	6.334	6.196	6.149	6.205	6.050	5.837	5.993	6.045	5.865	5.835
4	6.329	6.191	6.158	6.208	6.036	5.831	5.994	6.055	5.888	5.835
3	6.336	6.200	6.166	6.197	6.045	5.834	6.001	6.059	5.870	5.853
Mean	6.333	6.196	6.161	6.204	6.039	5.832	5.994	6.055	5.877	5.840
Standard Deviation	0.002	0.003	0.006	0.005	0.007	0.003	0.004	0.004	0.007	0.005

In Table 2, the values in each column represent the spectral shift starting position $d\lambda/2\pi \times \varphi_0(y)$ calculated by using interference fringe fitting. These values are all measured when the detector status is the same but the light intensity is different. From Table 2, when light intensity changes by more than 130%, the maximum uncertainty of the fitting spectral shift position is only 0.007 3 nm, which suggests that changes in light source radiance distribution only slightly affect the accuracy of interference fringe fitting.

Furthermore, to evaluate the effect of interference fringe fitting, we conducted an experiment to compare the interference fringe method with the spectral matching method. First, we fine-tuned the position of CCD in spectral dimension to simulate the spectral position change, and then, calculated the offset by using interference fringe fitting and spectral matching. Finally, we compared the calculated values with the offset measured by the mercury spectrum. The results are shown in Table 3 ~ 6.

Table 3 and 4 are a contrast between the offset calculated by interference fringe fitting and measured by the

spectral lines of mercury lamp. Tables 5 and 6 show the result obtained when we placed a PrNd glass before the halogen lamp and used its sharp absorption peak to calculate the offset by using spectral matching. Fig. 5 shows an image of a lamp with PrNd glass. The black bands in the horizontal direction are the absorption bands of PrNd glass.

According to these tables, the offset measured by mercury has the least RMSE and can be used as a standard to evaluate the other methods. For interference fringe fitting, the maximum mean deviation is 0. 136 nm and the maximum RMSE is 0. 009 3 nm, and for spectral matching that uses the absorptionpeak of PrNd glass, the maximum mean deviation is 0. 151 nm and the maximum RMSE is 0. 083 nm. The maximum deviation of interference fringe fitting is a litter lower than that of spectral matching, whereas the RMSE of interference fringe fitting
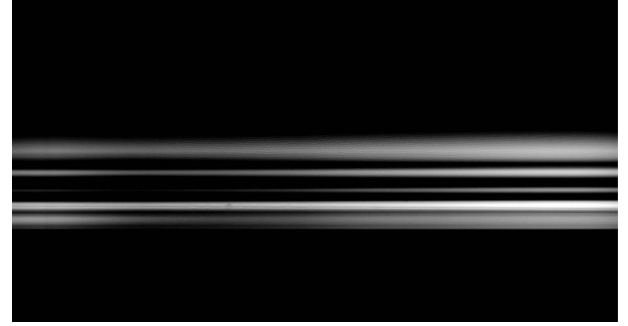

Fig. 5   Absorption of PrNd glass
图 5   镨铷玻璃吸收峰分布图

is a litter higher. These small differences are within the error range.

Table 3   Contrast of measured offset between interference fringe fitting and mercury lamps（three halogen lamps）
表 3   干涉条纹算法计算值和汞灯实测的谱线偏移值对比（三盏卤素灯光源）

Test No.		Column/nm											
		289	290	291	292	293	294	295	296	297	298	Mean	RMSE
3	fringes	−3.134	−3.099	−3.165	−3.163	−3.228	−3.295	−3.278	−3.136	−3.156	−3.203	−3.176	0.064
	Hg	−3.032	−3.026	−3.025	−3.055	−3.049	−3.074	−3.067	−3.101	−3.018	−3.119	−3.055	0.034
4	fringes	8.381	8.533	8.510	8.402	8.524	8.405	8.346	8.461	8.314	8.460	8.447	0.076
	Hg	8.409	8.419	8.366	8.374	8.433	8.385	8.433	8.376	8.497	8.399	8.407	0.039

Table 4   Contrast of measured offset between interference fringe fitting and mercury lamps（five halogen lamps）
表 4   干涉条纹算法计算值和汞灯实测的谱线偏移值对比（五盏卤素灯光源）

Test No.		Column/nm											
		289	290	291	292	293	294	295	296	297	298	Mean	RMSE
3	fringes	−6.124	−5.875	−5.928	−5.989	−6.018	−6.170	−6.104	−5.990	−5.962	−5.961	−6.009	0.093
	Hg	−6.002	−6.045	−5.990	−6.088	−5.998	−6.045	−5.975	−6.014	−5.940	−6.006	−6.016	0.041
4	fringes	4.133	4.342	4.300	4.183	4.389	4.158	4.276	4.345	4.270	4.286	4.273	0.085
	Hg	4.409	4.380	4.379	4.334	4.345	4.335	4.411	4.341	4.429	4.389	4.365	0.035

Table 5   Contrast of measured offset between spectral matching and mercury lamps（three halogen lamps）
表 5   传统吸收谱线拟合算法和和汞灯实测的谱线偏移值对比（三盏卤素灯光源）

Test No.		Column/nm											
		314	315	316	317	318	319	320	321	322	333	Mean	RMSE
5	PrNd	−3.387	−3.478	−3.562	−3.379	−3.462	−3.428	−3.415	−3.491	−3.315	−3.522	−3.455	0.074
	Hg	−3.501	−3.415	−3.466	−3.485	−3.464	−3.510	−3.494	−3.481	−3.536	−3.439	−3.481	0.035
6	PrNd	7.802	7.764	7.869	7.734	7.678	7.811	7.776	7.824	7.845	7.832	7.795	0.057
	Hg	7.913	7.876	7.919	7.927	7.965	7.884	7.932	7.964	7.917	7.892	7.920	0.030

Table 6   Contrast of measured offset between spectral matching and mercury lamps（five halogen lamps）
表 6   传统吸收谱线拟合算法和和汞灯实测的谱线偏移值对比（五盏卤素灯光源）

Test No.		Column/nm											
		314	315	316	317	318	319	320	321	322	333	Mean	RMSE
7	PrNd	−7.215	−7.269	−7.111	−7.345	−7.361	−7.314	−7.221	−7.348	−7.301	−7.339	−7.281	0.079
	Hg	−7.140	−7.113	−7.189	−7.112	−7.163	−7.125	−7.204	−7.068	−7.122	−7.108	−7.130	0.041
8	PrNd	4.241	4.168	4.286	4.117	4.381	4.226	4.234	4.102	4.170	4.165	4.207	0.083
	Hg	4.012	4.113	4.098	4.033	4.110	4.075	4.038	4.125	4.121	4.086	4.080	0.040

4   Summary

The light absorption efficiency of back-illuminated CCD devices decline sharply in the near-infrared band（about 750 nm to 1 000 nm）, which causes the incident light to reflect back and forth. Therefore, dispersive imaging spectrometers that use this kind of CCD observe in-

terference fringes in the near-infrared band. These fringes are sensitive to incident light wavelength and stable in spatial distribution. Thus, they are suitable for the measurement and calibration of slight spectrum shift.

In this paper, we constructed an optical resonator model and calculated the curve of fringe intervals changing from the wavelength of incident light. On this basis, we first used a band-pass filter to extract the fringe signal and then constructed a cosine function model for binomial fitting. Finally, we obtained the phase information of the interference fringes. When the spectral position changed, the values of spectral position change can be calculated by the difference between the phase positions.

We built a grating dispersion push-broom imaging spectrometer prototype that uses a back-illuminated CCD detector. With the test system that uses an integrating sphere as light source, we verified that interference fringe fitting is independent of the stability and strength of the light source, and calculated the reliability and precision of the method. The experiments show that when the incident light intensity changes by more than 130%, the maximum uncertainty of the fitting line positions is 0.007 3 nm. After the position of the spectrum is changed experimentally, compared with the result measured by mercury spectrum, the maximum error of spectrum position calculated by interference fringe fitting is 0.135 8 nm. These results suggest that interference fringe fitting can help the calibration system effectively reduce dependence on the stability of the light source, and improve the calibration accuracy of spectral position.

References

[1]XUE Qing-Sheng, Wang Shu-Rong, LU Feng-Qin. Study on Limb Imaging Spectrometer with Grating Dispersion [J]. Acta Optica Sinica, 2010,30(5): 1516－1521.

[2]PENG Zhi-Hong, ZHANG Chun-Ming, lufluence of depth of field on resolution of a microscope polarization interference imaging spectrometer [J]. Acta Optica Sinica, 2006,26(2): 239－243.

[3]ZHANG Chun-Ming, WANG Wei, XIANG Li-Bin, et al. Interference image spectroscopy for upper atmospheric wind field measurement [J]. Acta Optica Sinica, 2000,20(2): 234－239.

[4]XUE Qing-Sheng, HUANG Yu. LIN Guang-Yu. Optical System Design of Wide-Angle and High-Resolution Spaceborne Imaging Spectrometer [J]. Acta Optica Sinica, 2011,31(8): 0822001－1－0822001－6.

[5]ZHENG Yu-Quan. Precise spectral calibration for hyperspectral imager [J]. Optics and Precision Engineering,2010,11: 2347－2354.

[6]ZHANG Zhen-Duo, WANG Shu-Rong, LI Hong-Zhuang. Study on Calibration Environment of Spectral Responsivity for Space Ultraviolet Remote Sensing Instrument [J]. Acta Optica Sinica. . 2012,3: 0312001－1－0312001－8.

[7]Luis Guanter, Rudolf Richer, José Moreno. Spectral calibration of hy-

perspectral imagery using atmospheric absorption features [J]. Applied Optics, 2006,45(10): 2360－2370.

[8]KatrasnikJaka, BuermenMiran, PernusFranjo, et al. Spectral characterization and calibration of AOTF spectrometers and hyper-spectral imaging systems [J]. Chemometrics and Intelligent Laboratory Systems, 2010,101(1): 23－29.

[9]Xiong X, Chiang K, Esposito J, et al. MODIS on-orbit calibration and characterization [J]. Metrologia, 2003,40: 89－92.

[10]ZHANG Jun-Qiang, SHAO Jian-Bing, YAN Chang-Xiang. Data processing of on-orbit spectral calibration of space-borne high resolution imaging spectrometer [J]. Chinese Optics, 2011,4(2): 175－181.

[11]Pamela B, John S, Carol S. Hyperion on-orbit validation of validation of spectral calibration using atmospheric lines and an on-board system [C]. Proc. SPIE,4480: 231－235(2002).

[12]Hedman T R, Jarecke P J, Liao L B. Hyperspectral imaging spectrometer spectral calibration [J]. Patent, United State: 6, 111, 640, 2000－08－29.

[13]Green R O, Conel J E, Margolis J S, et al. In-flight validation and calibration of spectral and radiometric characteristics of the Airborne Visible/Infrared Imaging Spectrometer [C]. Imaging Spectroscopy of the Terrestrial Environment International Society for Optics and Photonics, 1990: 18－36.

[14]Green R O, Pavri B, Boardman J. On-orbit calibration of an ocean color sensor with an underflight of the Airborne Visible/Infrared Imaging Spectrometer (AVIRIS) [J]. Advances in Space Research, 2001, 28(1): 133－142.

[15]Gao B C, Montes M J, Davis C O. Refinement of wavelength calibrations of hyperspectral imaging data using a spectrum-matching technique [J]. Remote Sensing, Environ, 2004, 90(4): 424－433.

[16]CHEN Hong-Yao, ZHANG Li-Ming, LI Xin. Hyperspectral Sensor in Flight Spectral Calibration Based on Characteristic Spectral of Atmosphere [J]. Acta Optica Sinica, 2013, 33(5): 0528003－1－0528003－7.

[17]ZHENG Yu-Quan, YU Bing-Xi. Overview of spectrum-dividing technologies in imaging spectrometer [J]. Remote Sensing, 2002,6(1): 75－80.

[18]WANG Yi-Qun, YAN Chang-Xiang, MIAO Chun-An. Choise of spectral-splitting modes in space-borne hyper-spectral imager [J]. Chinese Optics and applied Optics, 2009,2(4): 304－308.

[19]KONG Ning-Ning, LI Chao, XIA Ming-Liang. Research on Flat Field Correction Method in Adaptive Optics Retinal Imaging System [J]. Acta Optica Sinica, 2011,12: 1211001－1－1211001－8.

[20]Kamata Yukiko, Miyazaki Satoshi, Nakaya Hidehiko. Evaluation of the fully-depleted back-illuminated CCD for Subaru Suprime-Cam [J]. SPIE Astronomical Telescopes + Instrumentation. International Society for Optics and Photonics, 2008: 70211S-70211S-9.

[21]Buckley D A H. SALT Calibration Requirements and CCD issues [J]. S. A. L. T, 9th, April, 2002.

[22]Paul Jerram, David Burt, NeiGuyatt. Back-thinned CMOS Sensor Optimisation [J]. OPTO. International Society for Optics and Photonics, 2010: 759813－759813－12.

[23]Koichi Okada, Etsuro Yokoyama, Hidetoshi Miike. Interference Fringe Pattern Analysis Using Inverse Cosine Function [J]. Electronics and Communications in Japan, Part 2, 2007, 90(1): 61－73.